

Supporting Information: Experimental Observation of ABCB Stacked Tetralayer Graphene

Konstantin G. Wirth,^{*,†} Jonas B. Hauck,[‡] Alexander Rothstein,^{¶,§} Hristiyana
Kyoseva,[¶] Dario Siebenkotten,[†] Lukas Conrads,[†] Lennart Klebl,[‡] Ammon
Fischer,[‡] Bernd Beschoten,[¶] Christoph Stampfer,^{¶,§} Dante M. Kennes,^{‡,||} Lutz
Waldecker,[¶] and Thomas Taubner^{*,†}

[†]*1st Institute of Physics (IA), RWTH Aachen University, 52074 Aachen, Germany*

[‡]*Institute for Theory of Statistical Physics, RWTH Aachen University and JARA
Fundamentals of Future Information Technology, 52062 Aachen, Germany*

[¶]*2nd Institute of Physics and JARA-FIT, RWTH Aachen University, 52074 Aachen,
Germany*

[§]*Peter Grünberg Institute (PGI-9), Forschungszentrum Jülich, 52425 Jülich, Germany*

^{||}*Max Planck Institute for the Structure and Dynamics of Matter, Center for Free Electron
Laser Science, 22761 Hamburg, Germany*

E-mail: konstantin.wirth@rwth-aachen.de; taubner@physik.rwth-aachen.de

S1 Stability and abundance

In Figure S1 the optical phase (Φ_3) and a Raman map of the 4LG flake labeled Flake 2 in the main text are shown over the course of several measurements. The phase image (Φ_3) in Figure S1 a) is recorded at a photon energy of 0.34 eV. The 4LG flake can be clearly distinguished from the SiO_2 substrate on the left (red area). Three regions on the 4LG are marked with their respective stacking. The domain with the weakest contrast towards the SiO_2 is ABCB and the strongest ABCA.

The Raman map around the 2D peak recorded after the s-SNOM measurements is depicted in Figure S1 b). The ABCA-domain shrunk in the middle of the image, while the ABCB-domain is still present. However, due to the limited resolution of the Raman setup, the exact shape of the domains is difficult to determine. Subsequent s-SNOM measurements repeated at 0.34 eV are depicted in Figure S1 c). The ABCA-domain has a similar size to what can be expected from the Raman in Figure S1 b), while the ABCB-domain shrunk again to a small stripe and a triangular feature at the right side of the image. This feature is indicated by a black dashed rectangle, which corresponds to the region investigated with IR nano-spectroscopy. In Figure S1 d) Raman spectra around the 2D peak corresponding to the map in Figure S1 b) are shown. The different domains exhibit similar features like in Figure 3 b).

In Figure S2 a) the topography of the 4LG flake labeled as Flake 3 in the main text is shown. The topography image of the 4LG is featureless, only a few dirt particles and the SiO_2 substrate can be identified, indicating a homogeneous number of four graphene layers.

In the corresponding optical amplitude (S_3) and phase image (Φ_3) in Figure S2 b) and c) recorded at a photon energy of 0.34 eV the flake can be clearly distinguished from the SiO_2 substrate. It shows three different amplitude and phase signals on the topographically featureless 4LG. The corresponding domains are indicated by ABAB, ABCA and ABCB. ABAB-domains cover the largest part of the 4LG. Two small domains of the largest contrast correspond to ABCA stacking. The triangular shaped ABCB-domain is located at the edge

between 4LG and the SiO₂ and has an amplitude signal between those of ABAB- and ABCA-domain. In the phase image in Figure S2 c) the same three domains can be identified. Again, the phase response is the largest with respect to the SiO₂ for the ABCA-domain and weakest for ABCB.

During our investigations, the domains of Flake 1 (main text) remained stable over several s-SNOM and Raman measurements (over the course of several weeks). For Flake 2 shown in Figure S1, however, we observed the consecutive collapse of a large ABCB domain to a small triangular shaped domains after Raman mapping at laser powers in the range of 3 mW. Such a change in the stacking order has been reported for TLG,¹ albeit for significantly higher laser power. The third investigated flake (Flake 3, Figure S2) also shows a triangular shaped similar sized domain of ABCB stacking, possibly a remnant of a collapsed larger domain. This argument is supported by investigations of the respective area with s-SNOM at a wavelength of 10.6 μm (Figure S2 d)), which reveals a small boundary like feature, indicated by the black box, similar to a shear soliton observed in bilayer graphene² and TLG.³ The energy barrier between ABCB and ABAB stacking is expected to be much lower compared to the transition from ABCA to ABAB.⁴ This instability might hamper device fabrication, because the ABCB stacking can transform to energetically favorable Bernal stacking, similar to metastable rhombohedral graphene upon stress or strain during device fabrication.⁵

S2 s-SNOM contrast calculation

The s-SNOM contrast for the 4LG/SiO₂/Si layer stack is calculated with the finite dipole model⁶ with an extension for layered samples⁷ as described in.⁸

The effective polarizability of the tip-sample system is calculated via

$$\alpha_{\text{eff}} = W_0^2 L \frac{\frac{2L}{a} + \ln \frac{a}{4eL}}{\ln \frac{4L}{e^2 a}} (2 + \eta_r(z)), \quad (\text{S1})$$

where a is the tip radius, L is the effective length of the assumed sphere and $W_0 = 1.31a$.

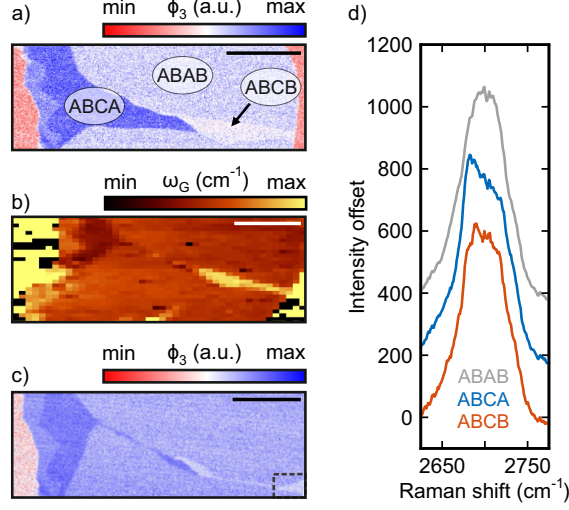


Figure S1: Flake 2: a) Optical phase (Φ_3) image of a 4LG flake on SiO₂, recorded first at 0.34 eV. b) Raman map around the 2D peak, recorded after the s-SNOM measurement with a high intensity Raman laser reveals a shrinkage of ABCA domain. c) Subsequent optical phase (Φ_3) image obtained at photon energies of 0.34 eV, after the Raman measurements, reveals a shrinkage of the ABCB domain when compared to b) and a). The dashed box indicates the region where s-SNOM nano-spectroscopy was conducted. d) Raman spectra recorded in the different regions for the three domains in b). The scalebars correspond to 5 μm each.

The detailed description of the model can be found in.^{6,7}

$$\eta_r(z) = \frac{\beta(2Lg - 2H - W_0 - a) \ln(\frac{4L}{4H+2W_0+a})}{4L \ln(\frac{4L}{a}) - \beta(4Lg - 4H - 3a) \ln(\frac{4L}{4H+2a})}, \quad (\text{S2})$$

where H is the tip height above the sample and g corresponds to a fraction of the total induced charge. The n -th Fourier component needs to be included to account for the higher harmonic demodulation of α_{eff} . The final amplitude and phase contrast depend solely on the third order Fourier component of $\eta_r(z)$ because the far-field coefficients can be neglected here.

$$\frac{S_3}{S_3^{\text{ref}}} = \frac{\text{Abs}[(\eta_3)]}{\text{Abs}[(\eta_3^{\text{ref}})]} \quad (\text{S3})$$

$$\Phi_3 - \Phi_3^{\text{ref}} = \text{Arg}[(\eta_3)] - \text{Arg}[(\eta_3^{\text{ref}})] \quad (\text{S4})$$

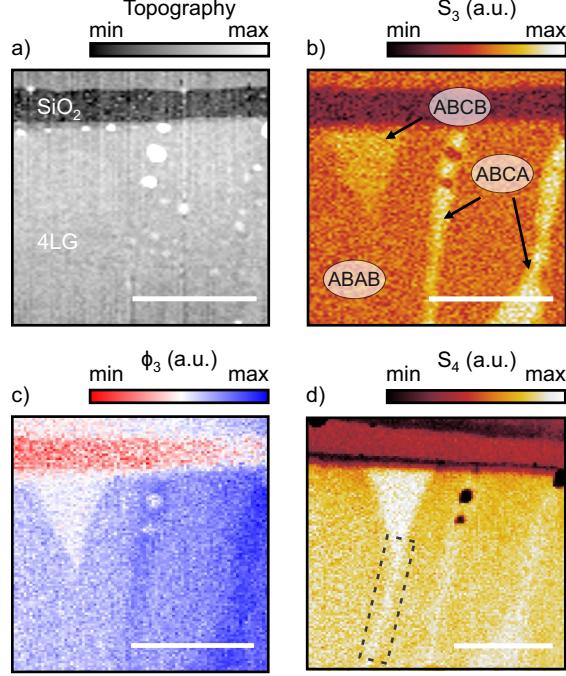


Figure S2: Flake 3: a) Topography image of the 4LG-only flake on SiO₂. b), c) Corresponding optical amplitude (S_3) and phase (Φ_3) images obtained at photon energies of 0.34 eV, revealing regions of different s-SNOM signal, with three different domains indicated by ABAB, ABCA and ABCB. The domains correspond to the same domains as in Figure 2 of the main text. d) Amplitude image obtained at 10.6 μm of the same area. A bright line below the ABCB domain is visible. The scale bar corresponds to 1 μm .

Parameters of the FDM are summarized in Table 1. We replace the electrostatic reflection coefficient β with a Fresnel reflection coefficient⁷ for a single dominant in-plane wave vector $k_{||} = 250000 \text{ cm}^{-1}$, comparable to the inverse of the expected tip radius of $\rho = 3.3 \cdot 10^5 \text{ cm}^{-1}$. To calculate the Fresnel coefficients for the stack, we use the transfer matrix method (TMM) for graphene layers with p-polarized light.⁹ In our model the tetralayer graphene is infinitesimal thin and a plane interface.

S3 s-SNOM contrasts for different chemical potentials

In Figure S3 a) and c) the optical conductivity of the three stackings is plotted, calculated for a broadening of $\eta = 40 \text{ meV}$ and chemical potentials μ of 20 and 100 meV, respectively. In b) and d) same amplitude and phase data as in Figure 4 are plotted for ABCB referenced

Table 1: FDM Parameter

Name	Value
Demodulation order n	3
Tapping Amplitude H	50 nm
L^6	300 nm
g^6	$0.7e^{i0.06}$
Tip radius a	30 nm
SiO ₂ thickness	90 nm

to ABAB. The calculated FDM spectra are shown for two different chemical potential. All three amplitude data sets show a higher peak at 0.38 eV, which can be either attributed to a smaller broadening or an increased chemical potential. For a change in the chemical potential, we expect a shift of the characteristic crossing of 1 and 0 in amplitude and phase, respectively. Furthermore, this also influences the contrast strength. A change in η would result in more pronounced features such as the peak in amplitude around 0.4 eV. For Flake 1 and Flake 2 the data fit better to 100 meV, especially the crossing of 1 in the amplitude is better reproduced. There are also indications for a smaller broadening, because amplitude data of Flake 1 indicate a sharper left flank and Flake 2 a more pronounced peak.

S4 Calculation of optical conductivity

For the calculation of the dynamic optical conductivity we employ the Kubo formula¹⁰

$$\sigma(\omega)_{i,j} = \frac{e^2 \hbar}{iS} \sum_{b_1, b_2, \mathbf{k}} \frac{n_f(e_{b_1}^{\mathbf{k}}) - n_f(e_{b_2}^{\mathbf{k}})}{e_{b_1}^{\mathbf{k}} - e_{b_2}^{\mathbf{k}}} \frac{\langle e_{b_1}^{\mathbf{k}} | \mathbf{v}_i | e_{b_2}^{\mathbf{k}} \rangle \langle e_{b_2}^{\mathbf{k}} | \mathbf{v}_j | e_{b_1}^{\mathbf{k}} \rangle}{\hbar\omega + e_{b_1}^{\mathbf{k}} - e_{b_2}^{\mathbf{k}} + i\eta}, \quad (\text{S5})$$

where $e_b(\mathbf{k})$ are the eigenenergies of the Hamiltonian in band b at momentum point \mathbf{k} and $|e_b^{\mathbf{k}}\rangle$ are the corresponding eigenvectors. The case of $e_{b_1}^{\mathbf{k}} = e_{b_2}^{\mathbf{k}}$ has to be considered separately and results in $\beta n_f(e_{b_1}^{\mathbf{k}})(n_f(e_{b_1}^{\mathbf{k}}) - 1)$. $\mathbf{v}_i(\mathbf{k})$ is the i -direction component of the velocity operator defined as $\mathbf{v}^n = \frac{i}{\hbar} [\mathbf{H}, \mathbf{x}^n]$ which can be expressed in the momentum-site basis as

$$\mathbf{v}_{o_1, o_2}^n = -\frac{i}{\hbar} \sum_{\mathbf{d}} e^{-i\mathbf{k}\mathbf{d}} H_{r_1, r_2 + \mathbf{d}} \cdot (r_{o_1}^n - r_{o_2}^n + \mathbf{d}^n), \quad (\text{S6})$$

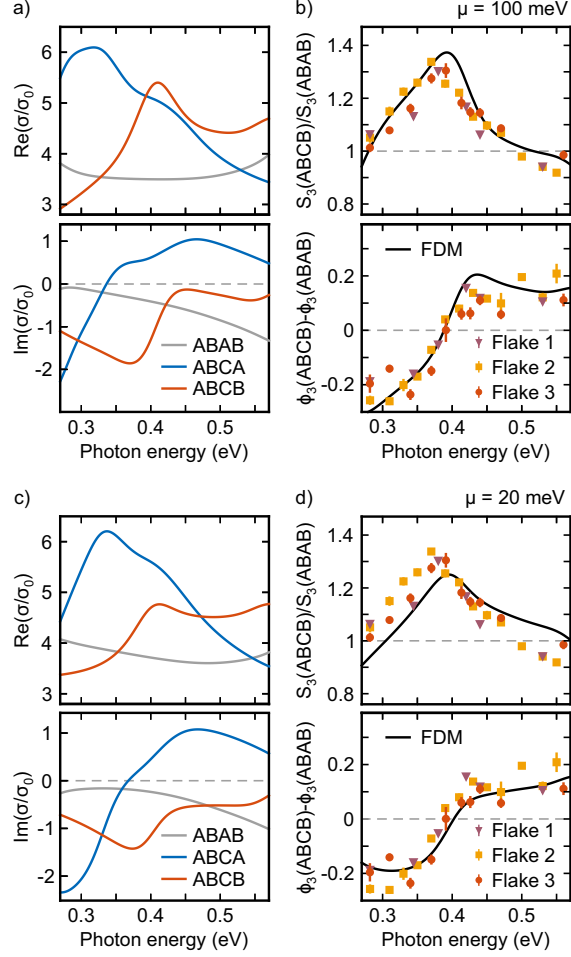


Figure S3: Optical conductivity data for ABCB plotted for $\mu = 20$ meV a) and $\mu = 100$ meV c). Comparison between experimental data for the three flakes and the modelled calculation for the chemical potentials.

with \mathbf{r}_i a vector pointing to a site i in the lattice and \mathbf{d} being a lattice vector. We chose the temperature to be room temperature (0.025 eV) and the broadening η as 40 meV. We chose a simple tight-binding Hamiltonian of the form

$$H = \sum_{i,j} \delta_{|\mathbf{r}_i - \mathbf{r}_j|, d_{cc}} \gamma_{\text{intra}} c_i^\dagger c_j + \delta_{|\mathbf{r}_i - \mathbf{r}_j|, d_{\text{layer}}} \gamma_{\text{inter}} c_i^\dagger c_j \quad (\text{S7})$$

consisting of only nearest-neighbor intralayer (in a distance $d_{cc} = 1.42 \text{ \AA}$) and nearest-neighbor interlayer hopping (in a distance $d_{\text{layer}} = 3.35 \text{ \AA}$) with hopping energies of $\gamma_{\text{intra}} = 3.16 \text{ eV}$ and $\gamma_{\text{inter}} = 0.39 \text{ eV}$. We shift the Fermi energy to 50 meV. The modeling parameters,

Fermi-energy and broadening η were tweaked for the best agreement with the experimental results.

For the calculations of the DOS and the bandstructure in Figure 1, we employ a Slonzecewski-Weiss-McClure (SWMC) Hamiltonian, with parameters chosen based on Ref.¹¹ summarized in Table 2. The Hamilton-matrix can be constructed as

$$H_{i,j}^y(\mathbf{k}) = \delta_{i,j}\delta_{i,A}\Delta_y + \sum_{u_1, u_2 \in \mathbb{Z}} \sum_n \delta_{d_{i,j}^{u_1, u_2}, d_n} e^{-i\mathbf{k}\mathbf{R}(u_1, u_2)} \gamma_n, \quad (\text{S8})$$

where i and j are site indices within the unit cell, y marks the type of the lattice and is either ABAB, ABCA or ABCB and $\delta_{i,A}$ is one if i is an A -site and 0 otherwise. u_1 and u_2 iterate over all unit cells in the infinite lattice, $\mathbf{R}(u_1, u_2)$ gives the vectorial distance between the unit cells and $d_{i,j}^{u_1, u_2}$ gives the distance between site i and the image of site j shifted by u_1 and u_2 unit-cell vectors. d_n is the real-space distance associated with each of the hopping parameters is listed in the third column of Table 2.

Table 2: SWMC model parameters

Name	Value in eV	Distance in Å
γ_0	2.553	1.42
γ_1	0.343	3.35
γ_2	-0.009	6.70
γ_3	0.18	4.16
γ_4	0.173	3.64
γ_5	0.018	6.85
Δ_{ABAB}	-0.003	0.0, A site
Δ_{ABCA}	0.0	0.0, A site
Δ_{ABCB}	-0.018	0.0, A site

The values for the Δ_y are chosen such that we roughly reproduce the low energy behavior of the bandstructures from Ref.⁴ Therefore, the model is a good representation of the low energy degrees of freedom near half-filling.

S5 FTIR measurements of tetralayer graphene

The optical properties of few layer graphene are determined by its optical conductivity, which differs between the different crystal polytypes.¹² Therefore, the stacking order in few layer graphene can be determined by infrared far-field spectroscopy^{12,13} in the range between 0.2 and 1 eV. The influence of environmental effects, such as doping, on the infrared response of tetralayer graphene is expected to be reduced compared to thinner flakes,¹² making far-field spectroscopy a reliable technique. Requirement for the investigation with this method, however, are domains of sufficient size due to the optical diffraction limit. Within a set of approximately 50 flakes scanned by Raman spectroscopy, we identified one suitable ABCB domain. The flake (shown in Figure S4 b) exhibits an ABCB domains of approximately 5 x 30 μm^2 , adjacent to both ABCA and ABAB stacking.

Fourier transform infrared spectroscopy (FTIR) measurements on the three flakes shown in S4 reveal the infrared response of ABAB, ABCA and ABCB stacking orders. All measurements were performed in reflection geometry as the flakes are exfoliated onto SiO_2/Si substrates. We calculate the fractional change of the reflectance as following:

$$\Delta R = \frac{R_{4LG} - R_s}{R_s}, \quad (\text{S9})$$

where R_{4LG} is the reflectance of the flake and R_s is the reflectance of the substrate. The resulting spectrum (Fig. S4a) of ABAB is mainly featureless and exhibits only two small peaks at 0.26 eV and above 0.6 eV. The ABCA stacking exhibits two peaks, a pronounced one at 0.27 eV and a weaker one at 0.37 eV. This is good agreement with literature data on ABAB and ABCA stacked 4LG.¹² The fractional reflectance of ABCB stacking has a peak at 0.425 eV, which can be distinguished from the higher energy peak of ABCA by a shift towards higher energy and a slightly higher amplitude. The prominent peak of ABCA at lower energies is absent. The peak at 0.425 eV agrees well with the peak position in the real part of the conductivity (c.f. Figure 4a). The same peak as in the ABAB stacking at

0.26 eV is also present, because the surrounding of the ABCB stacking consists mostly of ABAB stacking which also contributes to the signal due to the non perfect aperture and the diffraction limit of infrared radiation. The peaks in the FTIR spectra correspond to the splitting between the conduction bands and are thus unique for each stacking order.^{12,13} This is the same principle as for the s-SNOM measurements presented in Figure 2 of the main text, but lacking the sub-diffraction limit spatial resolution of s-SNOM.

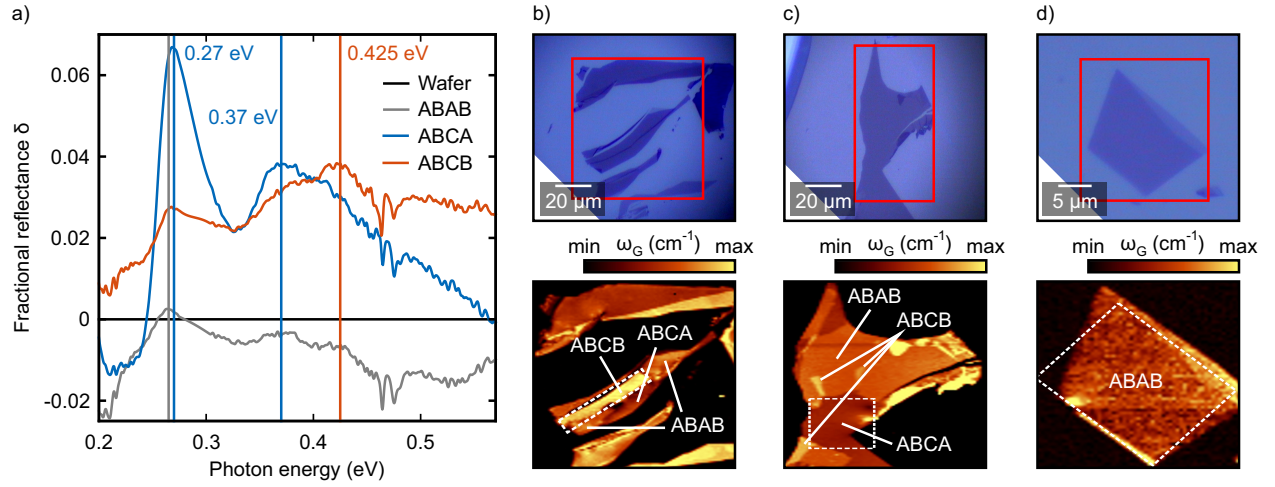


Figure S4: a) Fractional change of reflectance for three different stacking orders measured by FTIR with small apertures. The measurements were conducted under ambient condition. The CO₂ absorption peak between 0.27 and 0.3 eV was removed by interpolation. b), c) and d) Optical microscopy (top row) and Raman images (bottom row) of the investigated flakes. The red boxes in the optical images indicate the position of the Raman images. The white boxes in b), c) and d) indicate the areas (aperture position) where the FTIR spectra in a) were recorded. Different flakes were chosen to maximize the signal from the respective areas. Note that the flakes shown here are different from the ones shown in previous figures.

References

1. Zhang, J.; Han, J.; Peng, G.; Yang, X.; Yuan, X.; Li, Y.; Chen, J.; Xu, W.; Liu, K.; Zhu, Z.; Cao, W.; Han, Z.; Dai, J.; Zhu, M.; Qin, S.; Novoselov, K. S. Light-induced irreversible structural phase transition in trilayer graphene. *Light: Science & Applications* **2020**, *9*, 174.
2. Jiang, L.; Shi, Z.; Zeng, B.; Wang, S.; Kang, J.-H.; Joshi, T.; Jin, C.; Ju, L.; Kim, J.; Lyu, T.; Shen, Y.-R.; Crommie, M.; Gao, H.-J.; Wang, F. Soliton-dependent plasmon reflection at bilayer graphene domain walls. *Nature Materials* **2016**, *15*, 840–844.
3. Jiang, L.; Wang, S.; Shi, Z.; Jin, C.; Utama, M. I. B.; Zhao, S.; Shen, Y.-R.; Gao, H.-J.; Zhang, G.; Wang, F. Manipulation of domain-wall solitons in bi- and trilayer graphene. *Nature Nanotechnology* **2018**, *13*, 204–208.
4. Aoki, M.; Amawashi, H. Dependence of band structures on stacking and field in layered graphene. *Solid State Communications* **2007**, *142*, 123–127.
5. Geisenhof, F. R.; Winterer, F.; Wakolbinger, S.; Gokus, T. D.; Durmaz, Y. C.; Priesack, D.; Lenz, J.; Keilmann, F.; Watanabe, K.; Taniguchi, T.; Guerrero-Avilés, R.; Pelc, M.; Ayuela, A.; Weitz, R. T. Anisotropic Strain-Induced Soliton Movement Changes Stacking Order and Band Structure of Graphene Multilayers: Implications for Charge Transport. *ACS Applied Nano Materials* **2019**, *2*, 6067–6075.
6. Cvitkovic, A.; Ocelic, N.; Hillenbrand, R. Analytical model for quantitative prediction of material contrasts in scattering-type near-field optical microscopy. *Optics Express* **2007**, *15*, 8550.
7. Hauer, B.; Engelhardt, A. P.; Taubner, T. Quasi-analytical model for scattering infrared near-field microscopy on layered systems. *Optics Express* **2012**, *20*, 13173–13188.

8. Wirth, K. G.; Linnenbank, H.; Steinle, T.; Banszerus, L.; Icking, E.; Stampfer, C.; Giessen, H.; Taubner, T. Tunable s-SNOM for Nanoscale Infrared Optical Measurement of Electronic Properties of Bilayer Graphene. *ACS Photonics* **2021**, *8*, 418–423.
9. Zhan, T.; Shi, X.; Dai, Y.; Liu, X.; Zi, J. Transfer matrix method for optics in graphene layers. *Journal of Physics: Condensed Matter* **2013**, *25*, 215301.
10. Kubo, R. Statistical-Mechanical Theory of Irreversible Processes. I. General Theory and Simple Applications to Magnetic and Conduction Problems. *Journal of the Physical Society of Japan* **1957**, *12*, 570–586, eprint: <https://doi.org/10.1143/JPSJ.12.570>.
11. Grüneis, A.; Attacalite, C.; Wirtz, L.; Shiozawa, H.; Saito, R.; Pichler, T.; Rubio, A. Tight-binding description of the quasiparticle dispersion of graphite and few-layer graphene. *Phys. Rev. B* **2008**, *78*, 205425.
12. Mak, K. F.; Shan, J.; Heinz, T. F. Electronic Structure of Few-Layer Graphene: Experimental Demonstration of Strong Dependence on Stacking Sequence. *Physical Review Letters* **2010**, *104*, 176404.
13. Mak, K. F.; Sfeir, M. Y.; Misewich, J. A.; Heinz, T. F. The evolution of electronic structure in few-layer graphene revealed by optical spectroscopy. *Proceedings of the National Academy of Sciences* **2010**, *107*, 14999–15004.